Macromolecules **1997,** *30,* 1053−1068

Polymer Aggregates with Crystalline Cores: The System Polyethylene−Poly(ethylenepropylene)

D. Richter,* D. Schneiders, M. Monkenbusch, and L. Willner

Institut für Festkörperforschung, Forschungszentrum Jülich, 52425 Jülich, Germany

L. J. Fetters, J. S. Huang, and M. Lin

Exxon Corporate Research and Engeneering Corporation, Annandale, New Jersey 08801

K. Mortensen

Physics Department, Risø National Laboratory, 4000 Roskilde, Denmark

B. Farago

Institut Laue-Langevin, 38042 Grenoble Cedex, France

Received July 16, 1996; Revised Manuscript Received November 12, 1996⊗

ABSTRACT: We have studied the aggregation behavior of polyethylene−poly(ethylenepropylene) (PE−PEP) diblock copolymers dissolved in decane. For this purpose PE−PEP diblock copolymers of various molecular weights, compositions, and degrees of deuteration were synthesized via an anionic route. The structure and morphology of the aggregates was studied by small angle neutron scattering varying both the contrast as well as the polymer labeling. We found a hierarchy of structures: The PE component crystallizes in lamellar sheets (thickness 40−80 Å) surrounded on both sides by a PEP brush which exhibits a close to parabolic density profile. Different aggregates form macroaggregates of needlelike shape with the PE lamellar planes in the long direction. This macroaggregation is well described by a paracrystalline structure factor. The structural parameters depending on composition and molecular weights can be well understood in terms of a free energy of formation based on a scaling model. A quantitative evaluation of the different contributions to the free energy reveals an important role of defect structures resulting from the ethylene side branches in the polyethylene component. Finally, we show in a semiquantitative approach that the van der Waals energy between the brushes is large enough to facilitate macroaggregation.

1. Introduction

Diblock copolymers in selective solvents form micelles, a phenomenon similar to that of amphiphilic surfactants. Many groups have studied the micellar behavior in polymer systems where the micellarization is based on the incompatibility between one of the polymer components and the solvent.[1−3] Such experiments have been performed with a variety of techniques such as low angle and dynamic laser light scattering,[4−7] viscometry,[8−9] neutron small angle scattering (SANS),[10] and small angle X-ray scattering.[11,12] In these cases the insoluble part forms the liquid or amorphous core of the micellar structure. Particularly well-known is the polystyrene−polyisoprene−decane system.[13] Here, we have followed a different concept and studied a diblock copolymer system, where the driving force toward aggregation comes from the tendency of one of the components to crystallize. As a model system we have chosen the diblock copolymer polyethylene−poly(ethylenepropylene) (PE−PEP) in decane. By anionic polymerization well-defined diblock copolymers can be obtained via the precursor diblock polybutadiene−polyisoprene (PB−PI) which subsequently is hydrogenated. The polyethylene component crystallizes with high enthalpy gain and delivers the thermodynamic reason for aggregation. From the morphology of polyethylene crystals lamellar structures are expected with a crystalline polyethylene core surrounded by a poly(ethylenepropylene) brush. The detailed morphology of such aggregates shall be determined by the balance of entropic forces resulting from the stretching of the hairs and the enthalpic contribution from the polyethylene chain folding.

In this paper we present systematic investigations on the aggregation phenomena and in particular the morphologies of the aggregates occurring in this block copolymer system dissolved in decane. For this purpose we have synthesized a series of well-defined diblocks with different PE−PEP compositions and molecular weights. In order to facilitate detailed small angle neutron scattering investigations by contrast variation, these block copolymers were created with different hydrogen and deuterium contents in the different blocks. In section 2 we describe the sample preparation and characterization as well as the small angle neutron scattering measurements. Section 3 gives an outline of the models considered and develops an expression for the structure factor in order to describe the observed macroaggregation of the PE−PEP lamellae. In section 4 we report the experimental results commencing with light scattering measurements on the critical micellar concentration. Thereafter we highlight the structural models by visualizing their essential features on the partial scattering functions originating from core and brush scattering as well as for the structure factor resulting from interlamellar macroaggregation. In a next step quantitative multiparameter fits on data under various contrast conditions are presented. Measurements at different concentrations show an increasing degree of organization in the macroaggregates. Finally, shear experiments lead to an observation of the way the PE−PEP aggregates position themselves in the macroaggregate. Section 5 is devoted to a theoretical

---

⊗ Abstract published in *Advance ACS Abstracts,* February 1, 1997.

S0024-9297(96)01039-X CCC: $14.00

Table 1. Molecular Characteristics of the PE−PEP Diblock Copolymers: M_{PE} and M_{PEP} Molecular Weights of the Two Blocks; ζ_{PE}, ζ_{PEP} Corresponding Densities; ζ Average Density; ν_{PE} Polyethylene Fraction; m_s see Eq 16; ρ_{PE} and ρ_{PEP} Scattering Length Densities of the Two Blocks

	5DH8HH	5DD10HD	6HH10DH	6HH15DH[b]	6DH20HH	10DH16HH
M_{PE}	5000 ± 5%	5000 ± 5%	6000 ± 5%	6000 ± 5%	6000 ± 5%	10000 ± 5%
M_{PEP}	8000 ± 5%	10000 ± 5%	10000 ± 5%	15000 ± 5%	20000 ± 5%	16000 ± 5%
ζ_{PE}/g cm^{-3}	1.02 ± 0.02	1.06 ± 0.02	0.93 ± 0.02	0.93 ± 0.02	1.02 ± 0.02	1.02 ± 0.02
ζ_{PEP}/g cm^{-3}	0.86	0.89 ± 0.01	0.94 ± 0.01	0.94 ± 0.01	0.86	0.86
ζ/g cm^{-3}	(0.91 ± 0.01)[a]	(0.94 ± 0.01)[a]	(0.94 ± 0.01)[a]	(0.94 ± 0.01)[a]	0.89 ± 0.01	(0.91 ± 0.01)[a]
ν_{PE}	0.34 ± 0.02	0.30 ± 0.02	0.38 ± 0.02	0.29 ± 0.02	0.20 ± 0.02	0.34 ± 0.02
m_s	0.95 ± 0.07	1.19 ± 0.09	0.82 ± 0.06	1.43 ± 0.19	1.99 ± 0.15	0.95 ± 0.07
$\rho_{PE}/10^{10}$ cm^{-2}	5.28 ± 0.63	7.98 ± 0.17	−0.33 ± 0.01	−0.33 ± 0.01	5.28 ± 0.63	5.28 ± 0.63
$\rho_{PEP}/10^{10}$ cm^{-2}	−0.31	1.99 ± 0.77	5.06 ± 0.77	5.06 ± 0.77	−0.31	−0.31

[a] Calculated value confirmed by density gradient column measurements. [b] The molecular weight of the PEP component was determined from absolute scattering intensities obtained in the SANS measurements.

assessment of the observed structures. In terms of a thermodynamic model based on scaling considerations, an expression for the aggregate free energy is derived, leading to a number of scaling relations. These relations are compared to the experimental observations. Thereafter a quantitative evaluation of the different contributions to the free energy make it clear that defect structures induced by the ethyl branches of the PE chains dominate the crystallization process. Considering the reason for macroaggregation, the van der Waals interaction between different large platelets is calculated, yielding sufficient attraction to overcome the translational entropy. The order of magnitude of this van der Waals interaction is related to the threshold shear rate beyond which the macroaggregates disintegrate.

2. Experimental Section

2.1. Samples. In order to obtain well-defined molecular weights and structures, anionic polymerization is a convenient route of synthesis. For polyolefins this requires a two-step procedure. In the first step polydiene mother polymers are synthesized, which, in a second step, are saturated by hydrogenation. The detailed experimental procedures for anionic polymerization have been described elsewhere.[14,15] In the present case *sec*- or *tert*-butyllithium was used as the initiator. All manipulations were performed in evacuated glass reactors with break-seals and constrictions. The polybutadiene−polyisoprene (PB−PI) diblock copolymers were obtained by polymerization of 1,3-butadiene and 2-methyl-1,3-butadiene in nonpolar hexane, yielding mainly 1,4 addition. The molecular weights of the first synthesized PB block and of the full polymer were characterized by low angle laser light scattering (LALLS) using a chromatics KMX6 low angle laser photometer and by size exclusion chromatography employing a Waters 150 C instrument. The thus synthesized diblock copolymers were saturated by hydrogenation at 80−100 °C under a pressure of 25−30 bar using palladium on barium sulfate as a catalyst, which yielded the desired polyethylene−poly(ethylenepropylene) (PE−PEP) diblock copolymers.

Detailed studies of the structure and morphology of polymer systems by small angle neutron scattering (SANS) require the variation of the scattering properties of the different polymer components by varying the degree of hydrogenation or deuteration, respectively. In the present case, two options were used. (i) The precursor PB−PI diblocks were synthesized with hydrogenated and deuterated components, respectively, and (ii) the saturation step was undertaken using either hydrogen or deuterium gas. The obtained molecular weights and sample compositions are displayed in Table 1. The nomenclature *X*ij*Y*kl is defined as follows: *X* = molecular weight of the PE block; i = H, D describes the isotope composition of the underlying butadiene monomer; j = H, D is the type of saturation by either hydrogen or deuterium gas; *Y* gives the molecular weight of the PEP component; k, l denote again the isotope composition of the monomer as well as the saturation gas.

Table 2. Nomenclature Used for the Different Ways of Hydrogenation and Deuterations and Obtained H/D Content

precursor polymer	saturation	nomenclature	H/D contents
HPB	H	HH PE	8/0
	D	HD PE	5.4 ± 0.6/2.6 ± 0.6
DPB	H	DH PE	2.6 ± 0.6/5.4 ± 0.6
	D	DD PE	0/8
	H	HH PEP	10/0
	D	HD PEP	7 ± 1/3 ± 1
DPI	H	DH PEP	3 ± 1/7 ± 1
	D	DD PEP	0/10

For a quantitative evaluation of SANS data, the exact knowledge of the scattering length densities ρ_p of the different polymer components is crucial

$$\rho_p = \frac{\sum b_i}{v_p} \qquad (1)$$

where b_i are the scattering lengths of the different atoms in a monomer and v_p is the monomer volume. While the evaluation of v_p is straightforward for the solubilized PEP component, it is more involved for the crystallizable PE. Furthermore, in the case of mixed isotope contents there exist also uncertainties in the exact isotope compositions. Two effects relating to the sample preparation have to be considered. (i) The density of the polyethylene crystal reflected by v_p depends on the ethyl branch contents. If polyethylene is obtained from saturation of 1,4-polybutadiene, about 18 ethyl branches per 1000 main chain PE bonds remain from the 1,2 addition of polybutadiene monomers. Several authors have studied the crystalline polyethylene density ζ_{PE} as a function of the ethyl branch number.[16,17] From these results $\zeta_{PE} = 0.93 \pm 0.02$ g/cm^3 for our situation can be estimated. In several cases these estimated densities have been verified by density gradient column measurements on our samples (see Table 1). (ii) Hydrogenation using hydrogen gas of a different isotope than the underlying polymer yields, besides the addition of two hydrogens or deuterons at the double bond, further isotope exchange reactions of other hydrogens or deuterons of the monomer; e.g., for the deuteration of hydrogenated polybutadiene, Tanzer et al.[18] found a final composition of $C_4H_{4.8}D_{3.2}$, indicating an exchange of 1.2 extra protons. Similarly, also in the case of PI, Almdal et al.[19] have observed exchange reactions indicating a substitution of 2−3 extra protons. Here, from the SANS experiments at different solvent contrasts the amount of H−D substitution for the various compositions could be obtained. The results are displayed in Table 2.

The scattering experiments were performed on polymer solutions with polymer volume fractions Φ between 0.5% and 10%. The samples were prepared by an addition of the required polymer fractions and solvent with the selected isotope composition by weighing. Thereafter, the samples were heated to 70 °C (a temperature above the solubilization temperature of the PE fraction in decane). Independent of concentration, optically clear solutions were found. These samples were then slowly cooled to room temperature (cooling rate about 1 deg/min). At room temperature the solutions had a light bluish color and showed a strong increase of viscosity, indicating aggregation of polymers. Above 5% volume fraction gels were obtained. All samples were filled into quartz cells providing 1 or 2 mm thickness.

2.2. Small Angle Neutron Scattering. In this work we consider exclusively scattering from PE–PEP diblock aggregates in solution. The scattering cross section is then determined by the spatially varying polymer density profiles $c_{\mathrm{PEP}}(r) \equiv c_{\mathrm{b}}(r)$ and $c_{\mathrm{PE}}(r) \equiv c_{\mathrm{c}}(r)$ weighted by the corresponding scattering contrast factors $\Delta\rho_{\mathrm{b,c}}$ with respect to the solvent.

$$\Delta\rho_{\mathrm{b,c}} = \rho_{\mathrm{b,c}} - \rho_{\mathrm{s}} \tag{2}$$

Thereby $\rho_{\mathrm{b,c,s}}$ are defined according to eq 1. In these terms the macroscopic scattering cross sections can be formulated

$$\frac{\mathrm{d}\Sigma}{\mathrm{d}\Omega}(Q) = \frac{1}{V}\left|\int_V [\Delta\rho_{\mathrm{b}} c_{\mathrm{b}}(\underline{r}) + \Delta\rho_{\mathrm{c}} c_{\mathrm{c}}(\underline{r}) + \rho_{\mathrm{s}}]\mathrm{e}^{\mathrm{i}\underline{Q}\underline{r}}\,\mathrm{d}^3\underline{r}\right|^2 \tag{3}$$

Thereby, the integration is performed over the sample volume V, $Q = 4\pi/\lambda \sin\theta$ is the scattering vector, where θ is the scattering angle and λ is the neutron wavelength. Equation 3 can be reformulated in terms of partial scattering functions $S_{\mathrm{jj'}}(Q)$.[20]

$$\frac{\mathrm{d}\Sigma}{\mathrm{d}\Omega}(Q) = \Delta\rho_{\mathrm{b}}^{\,2} S_{\mathrm{bb}}(Q) + 2\Delta\rho_{\mathrm{b}}\Delta\rho_{\mathrm{c}} S_{\mathrm{bc}}(Q) + \Delta\rho_{\mathrm{c}}^{\,2} S_{\mathrm{cc}}(Q) \tag{4}$$

with

$$S_{\mathrm{jj'}}(Q) = \frac{1}{V}\int_V\int_V c_{\mathrm{j}}(\underline{r})c_{\mathrm{j'}}(\underline{r'})\exp[i\underline{Q}(\underline{r} - \underline{r'})]\,\mathrm{d}^3\underline{r}\,\mathrm{d}^3\underline{r'} \tag{5}$$

The partial scattering functions contain the structural information on the polymer aggregates and their mutual interaction. They, in principle, can be accessed separately by proper variation of the solvent scattering length density ρ_S, thereby varying the contrast factors of eq 2. When an experiment on an identical polymer using m different isotope mixtures for the solvent is performed, eq 4 yields a set of linear equations relating the measured intensities, the scattering contrasts, and the partial scattering functions.

$$\underline{\Sigma} = \underline{\underline{M}}\,\underline{S} \tag{6}$$

with the matrix

$$\underline{\underline{M}} = \begin{pmatrix} \Delta\rho_{\mathrm{b}_1}^{\,2} & 2\Delta\rho_{\mathrm{b}_1}\Delta\rho_{\mathrm{c}_1} & \Delta\rho_{\mathrm{c}_1}^{\,2} \\ \vdots & \vdots & \vdots \\ \Delta\rho_{\mathrm{b}_m}^{\,2} & 2\Delta\rho_{\mathrm{b}_m}\Delta\rho_{\mathrm{c}_m} & \Delta\rho_{\mathrm{c}_m}^{\,2} \end{pmatrix} \tag{7}$$

and the vectors

$$\underline{\Sigma} = \begin{pmatrix} \left.\frac{\mathrm{d}\Sigma}{\mathrm{d}\Omega}\right|_1 \\ \vdots \\ \left.\frac{\mathrm{d}\Sigma}{\mathrm{d}\Omega}\right|_m \end{pmatrix}; \qquad \underline{S} = \begin{pmatrix} S_{\mathrm{bb}}(Q) \\ S_{\mathrm{bc}}(Q) \\ S_{\mathrm{cc}}(Q) \end{pmatrix} \tag{8}$$

Equation 6 can be regrouped in terms of the known quantities $\rho_{\mathrm{s_i}}$ and $\underline{\Sigma}_{\mathrm{i}}$ yielding a quadratic regression problem

$$A - B\rho_{\mathrm{s_i}} + C\rho_{\mathrm{s_i}}^{\,2} = \left(\frac{\mathrm{d}\Sigma}{\mathrm{d}\Omega}\right)_{\mathrm{i}} \tag{9}$$

with

$$\begin{aligned} A(Q) &= \rho_{\mathrm{b}}^{\,2} S_{\mathrm{bb}}(Q) + 2\rho_{\mathrm{b}}\rho_{\mathrm{c}} S_{\mathrm{bc}}(Q) + \rho_{\mathrm{c}}^{\,2} S_{\mathrm{cc}}(Q) \\ B(Q) &= 2\rho_{\mathrm{b}} S_{\mathrm{bb}}(Q) + 2(\rho_{\mathrm{b}} + \rho_{\mathrm{c}}) S_{\mathrm{bc}}(Q) + 2\rho_{\mathrm{c}} S_{\mathrm{cc}}(Q) \\ C(Q) &= S_{\mathrm{bb}}(Q) + 2S_{\mathrm{bc}}(Q) + S_{\mathrm{cc}}(Q) \end{aligned}$$

From the quadratic regression analysis the best values for A, B, and C can be obtained for each Q. For this purpose the Q-dependent least squares analysis was performed. With the knowledge of these quantities the desired partial form scattering functions can be calculated, yielding

$$\begin{aligned} S_{\mathrm{bb}}(Q) &= \frac{A - B\rho_{\mathrm{c}} + C\rho_{\mathrm{c}}^{\,2}}{(\rho_{\mathrm{b}} - \rho_{\mathrm{c}})^2} \\ S_{\mathrm{bc}}(Q) &= \frac{A - B(\rho_{\mathrm{b}} + \rho_{\mathrm{c}})/2 + \rho_{\mathrm{b}}\rho_{\mathrm{c}}C}{(\rho_{\mathrm{b}} - \rho_{\mathrm{c}})^2} \\ S_{\mathrm{cc}}(Q) &= \frac{A - B\rho_{\mathrm{b}} + C\rho_{\mathrm{b}}^{\,2}}{(\rho_{\mathrm{b}} - \rho_{\mathrm{c}})^2} \end{aligned} \tag{10}$$

We note that independent of the number of solvent contrasts m, contrast variation does not give simultaneous information both on the scattering length densities ρ_{b} and ρ_{c} and on the partial scattering functions—for any choice, e.g., of ρ_{c}, solutions for S_{ij} can be found. In order to remove the uncertainties in ρ_{b} and ρ_{c} resulting from isotope exchange during hydrogenation and reduced crystallization density of PE due to ethyl branching, experiments on nearly identical diblocks with different H–D labeling are necessary. They have been performed for the low M_{W} materials. With the condition of consistent structures, the values for ρ_{c}, ρ_{b}, and ζ_{PE} quoted above were obtained.

These small angle neutron scattering (SANS) experiments were performed using the facilities at the National Institute for Standards and Technology in Gaithersburg, MD (5DH8HH, 10DH16HH), at the Laboratoire Léon Brillouin in Saclay, France (5DD10HD), and at the Institute Laue Langevin in Grenoble, France (other samples). Furthermore, shear experiments were undertaken at the SANS facility in Risø, Denmark.

All experiments were carried out at room temperature. Depending on the facility, the scattering vector was covering $0.0008\ \text{Å}^{-1} < Q < 0.12\ \text{Å}^{-1}$. This Q range was achieved by using different wavelengths and different sample to detector distances.

The raw data were corrected for the background from the solvent, the cell, and other sources which was measured with a blocked neutron beam. All the two-dimensional scattering patterns for isotropic conditions were radially averaged and calibrated to an absolute standard in order to get absolute units. Finally, incoherent scattering contributions due to the protonated polymer fractions were calculated and subtracted. The raw data are smeared by the instrumental resolution relating to the wavelength distribution $\Delta\lambda/\lambda$ the beam collimation, and the detector pixel sizes. These resolution effects were taken into account by proper convolution procedures.

3. Scattering Properties of Systems Containing Thin Plates

Guided by the crystallization properties of PE, we expect that under crystallization conditions for polyethylene PE–PEP diblock copolymers in solution form lamellar structures containing crystalline PE cores, which are solubilized by a PEP brush on both sides of the PE lamella. In the following we work out the scattering function of such a lamellar structure. In a second step we consider effects of platelet association, which may be driven by the attractive van der Waals interaction between different platelets.

3.1. Scattering from a Lamellar PE–PEP Core Brush Structure. We start considering the scattering from an infinite thin sheet. In reciprocal space the scattering intensity from such a sheet is concentrated on a line (Bragg rod) through the origin perpendicular to the plane of the sheet. If the sample is isotropic, containing an ensemble of randomly oriented sheets, then only those sheets contribute to the scattered intensity for which the direction of the sheet normal coincides with the direction of Q. The necessary angular average is easier to visualize, if it is viewed from a coordinate system attached to the plates. The angular averaging then results in the distribution of the detection element on a sphere with radius Q. For an isotropic sample the sphere is homogeneously covered by the detection element probability. Therefore the detection probability density on the sphere is inversely proportional to its surface, i.e. proportional to Q^{-2}. The cut of the Bragg rod with the detection element sphere yields a constant multiplied by the Q^{-2} density on the sphere, e.g. the scattering intensity due to a plane is $\propto 1/Q^2$. The divergence at $Q \to 0$ is an artifact due to the assumption of infinite lateral extension.

Now we consider a sheet with a finite lateral extension R (disk), much larger than the sheet thickness. In reciprocal space this finite extension leads to a broadening of the Bragg rod in the order of $1/R$. The orientationally averaged intensity from such a disk is given by

$$I(Q) = \int_0^{\pi/2} \left| \frac{2\pi R^2 J_1(QR \sin\vartheta)}{QR \sin\vartheta} \right|^2 \sin\vartheta \, \mathrm{d}\vartheta \qquad (11)$$

Thereby J_1 is the cylindrical Bessel function of first order. With the approximation

$$\left| \frac{J_1(QR \sin\vartheta)}{QR \sin\vartheta} \right|^2 \approx \frac{1}{4} \exp\left[-\left(\frac{1}{2} QR \sin\vartheta \right)^2 \right] \qquad (12)$$

eq 11 can be solved analytically yielding

$$I(Q) = (\pi R^2)^2 \frac{D(QR/2)}{QR/2} \qquad (13)$$

with the Dawson function

$$D(u) = \exp(-u^2) \int_0^u \exp(t^2) \, \mathrm{d}t \qquad (14)$$

$D(u)$ exhibits the following asymptotic behavior: For $u \to \infty$, $2D(u)/u \to 1/u^2$ and for $u \to 0$, $D(u)/u \to 1$; i.e. eq 13 interpolates between a constant finite forward scattering and the asymptotic high Q behavior proportional $1/Q^2$. Thus, by the above procedure the divergence of the scattering intensity for $Q \to 0$ is removed.

If the lateral shape of the platelets is elongated—any noncircular shape is elongated—the above treatment needs further modifications. In the limit of a very anisotropic shape, the Bragg rods look like a flat beam, and as soon as the Q sphere is smaller than the width of this beam but large compared to its thickness, a Q range with properties of scattering from a line, i.e., proportional Q^{-1}, interpolates between the Q^{-2} sheet scattering regime and the Q^0 particle scattering regime. However, as long as the smaller lateral platelet dimension is still larger than the distance corresponding to the smallest experimentally accessible Q value, the simple Dawson function formula is sufficient to account for an average lateral extension. Its main effect is the removal of divergence influences on the resolution convolution.

As long as size effects (R) and lamellar thickness are well separated in length scale for the consideration of density profiles across the sheet structure, we may treat the sheets as infinite; i.e., in the Q range, where the varying polymer density across the sheet width is important, the Bragg rods can be considered as infinitely thin. In such an extended sheet the polymer density varies only perpendicular to the sheet surface and modulates the Bragg rod intensity by a form factor resulting from these densities.

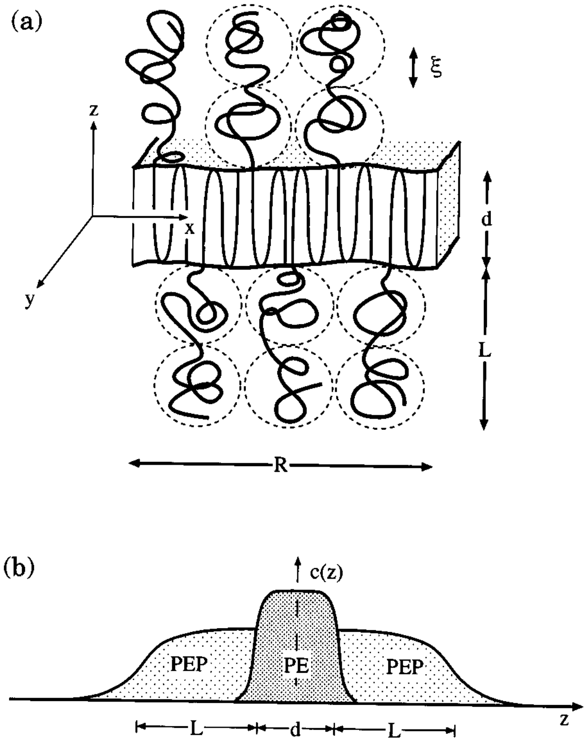

Figure 1. (a) Schematic sketch of the structure of a single lamella PE−PEP aggregate in decane. d denotes the core thickness, L the brush length, ξ the average blob size, and R the lateral dimension. (b) Corresponding concentration profiles $c(z)$ perpendicular to the aggregate plane.

$$\begin{aligned} P(Q) &= \left| \int_{-\infty}^{+\infty} [\Delta\rho_b(z) c_b(z) + \Delta\rho_c c_c(z)] \mathrm{e}^{\mathrm{i}Qz} \, \mathrm{d}z \right|^2 \\ &= |\Delta\rho_b c_b(Q) + \Delta\rho_c c_c(Q)|^2 \\ &= \Delta\rho_b^{\,2} P_{bb}(Q) + 2\Delta\rho_b \Delta\rho_c P_{bc}(Q) + \Delta\rho_c^{\,2} P_{cc}(Q) \end{aligned} \qquad (15)$$

$c_b(z)$ and $c_c(z)$ are the polymer density profiles within the brush and the core, respectively. $c_b(Q)$ and $c_c(Q)$ are the corresponding Fourier-transformed entities. $P_{bb}(Q)$, $P_{cc}(Q)$, and $P_{bc}(Q)$ are partial form factors associated with the brush and the core and an interference term, respectively. In order to illustrate such density profiles, schematically Figure 1a displays a cut through such a lamella sheet consisting of a PE core of thickness d and a PEP brush of length L. Figure 1b presents the corresponding density profiles.

We model the profile for the PE core by a rectangular shape convoluted by a Gaussian which has the effect of rounding the edges. In one approach we treat the brush in the same way. Such a profile allows a continuous variation between a rectangular structure which is close to the Alexander[21] and de Gennes,[22] brush and a profile nearer to a parabolic structure predicted by Milner et al.[23] In addition, we also explicitly consider parabolic profiles. For the rounded rectangles the Fourier-transformed profiles become

$$\begin{aligned} c_c(Q) &= d \frac{\sin Qd/2}{Qd/2} \exp\left(-\frac{1}{2} Q^2 \sigma_d^{\,2} \right) \\ c_b(Q) &= m_s \frac{d}{L} \left[2\left(L + \frac{d}{2} \right) \frac{\sin Q(L + d/2)}{Q(L + d/2)} \right. \\ &\quad \left. \exp\left(-\frac{1}{2} Q^2 \sigma_L^{\,2} \right) - d \frac{\sin Qd/2}{Qd/2} \exp\left(-\frac{1}{2} Q^2 \sigma_d^{\,2} \right) \right] \end{aligned} \qquad (16)$$

Thereby, L is the rectangular brush length and σ_L and σ_d are the Gaussian widths of the brush and core, respectively. The factor $m_s d/L$ describes the PEP fraction in the brush. m_s follows from geometric consideration and amounts to $m_s = \zeta_{\rm PE}M_{\rm PEP}/(2\zeta_{\rm PEP}M_{\rm PE})$. For a parabolic concentration profile from the geometrical boundary conditions we have

$$c_{\rm b}^{\rm P}(z) = \begin{cases} \frac{3}{2} m_{\rm s}\frac{d}{L_{\rm p}}\left(1 - \frac{1}{L_{\rm p}^2}\left(z - \frac{d}{2}\right)^2\right) & d/2 \le z \le L_{\rm p} + d/2 \\ 0 & \text{otherwise} \end{cases} \qquad (17)$$

Fourier transformation yields the Q-dependent profile $c_{\rm b}^{\rm P}(Q)$.

Finally combining eqs 13 and 15 yields the total macroscopic cross section of a disklike PE–PEP platelet.

$$\frac{{\rm d}\Sigma}{{\rm d}\Omega}(Q) = \phi\frac{\nu_{\rm PE}}{V_{\rm PE}}P(Q)(\pi R^2)^2\frac{D(QR/2)}{(QR/2)} \qquad (18)$$

The prefactor $\nu_{\rm PE}/V_{\rm PE}$ results from the normalization of the scattering intensity to the scattering volume where ϕ is the total polymer volume fraction $\nu_{\rm PE}$ is the relative fraction of PE in the diblock, and $V_{\rm PE} = \pi R^2 d$ is the scattering volume of the PE core.

3.2. Structure Factor of Stacks of Aggregates. The above considerations apply for single independent randomly oriented platelets immersed in the sample volume. If there is a slight attractive interaction between extended platelets which may be provided by the van der Waals forces, the summation over the large platelet areas may easily lead to interaction energies above many $k_{\rm B}T$ and therefore give rise to the formation of stacks of parallel platelets. The effect of such a "macroaggregation" on the scattering intensity is the appearance of a structure factor arising from the interplatelet interference which has to be multiplied by the single platelet scattering function. For a perfect stack the intensity distributed along the Bragg rods would condense into points on the rods, the distance between which is $G = \Delta Q_{\rm normal} = 2\pi/D$ where D is the stacking period in real space and G would be the corresponding reciprocal lattice vector. For random oriented staples the scattering pattern would be a sequence of Debye–Scherrer rings. Considering a random variation in the distance of neighboring platelets we treat the arising structure factor in terms of a one-dimensional paracrystalline structure.[24] Assuming a Gaussian probability distribution of the next neighbor distance leads to a distribution function

$$w_n(z,D) = \frac{1}{\sqrt{\pi n \sigma_D^2}}\exp\left[-\frac{1}{n}\frac{(z - nD)^2}{\sigma_D^2}\right] \qquad (19)$$

for the nth neighbor distance z because of the convolution properties of Gaussian distributions. Fourier transformation of the one-dimensional Patterson function $\Sigma w_n(D)$ leads to

$$S(Q) = \sum_{n=-\infty}^{\infty} {\rm e}^{{\rm i}QDn - nQ^2\sigma_D^2/4} = \frac{\sinh(Q^2\sigma_D^2/4)}{\cosh(Q^2\sigma_D^2/4) - \cos(QD)} \qquad (20)$$

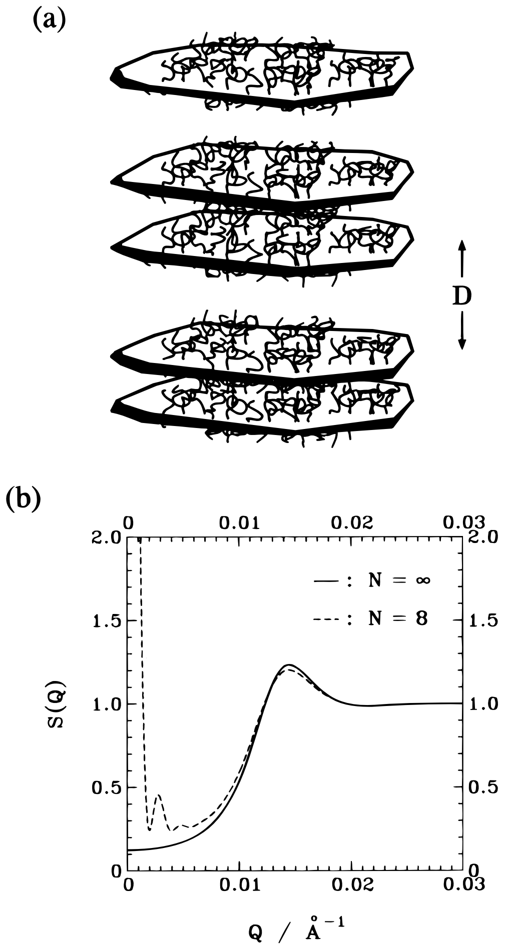

Figure 2. (a) Schematic sketch of an aggregate stack. (b) Resulting structure factors $S_N(Q)$ for a finite and $S(Q)$ for an infinite staple calculated for an average interlamellar distance of $D = 400$ Å and a Gaussian smearing of $\sigma_D = 200$ Å.

where $S(Q)$ is the structure factor for one-dimensional paracrystalline order. It is easily verified that $S(Q \to \infty) = 1$, as required for the structure factor of any disordered system. The effect of the distance variation is a dephasing of the interference terms, reducing their effect after ensemble averaging. For high enough Q the interference is completely destroyed. The same effect may occur by a random mutual tilt of different platelets in a stack, resulting in a tilt of the corresponding Bragg rods. The scattering from any two platelets can only interfere if their Bragg rods overlap. It is easily imagined that for thin Bragg rods this overlap goes to zero with increasing Q as soon as they are not perfectly parallel. The effect of this additional interference loss is not readily discernible from the dephasing due to distance variations. Therefore, in the following we consider such effects as included in the σ_D value which may come out larger than what would be expected due to pure distance variations.

The above treatment implies a homogeneous filling of space by a stack or at least very large stacks. This is not compatible with the macroscopically homogeneous appearance of sample solutions even at intermediate concentrations. It has to be inferred that, if any, finite size stacks form, implying a further modification of $S(Q)$. For a finite stack eq 20 changes to

$$S_N(Q) = 1 + \frac{2}{N}\sum_{n=1}^{N}(N - n)\cos(QDn){\rm e}^{-Q^2\sigma_D^2 n/4} \qquad (21)$$

where N is the number of stacking platelets. $S_N(Q)$ may be understood as a convolution of $S(Q)$ of eq 20 with a rectangular profile the width of which corresponds to the height of the staple. Thereby, the $\delta(Q)$ function representing the forward scattering in eq 20 that is usually invisible and has been ignored in $S(Q)$ now becomes visible and yields a narrow intensity distribution around $Q = 0$. For large distance variation σ_D this is the only significant effect of the convolution. Figure 2a illustrates such a staple of platelets. Figure 2b compares $S_N(Q)$ and $S(Q)$. The main effect of the structure factor is a strong suppression of intensity at low Q ($Q < 2\pi/D$); finite stapling leads to strongly increasing intensities below $Q < 2\pi/(ND)$.

3.3. Scattering from Internal Brush Structures—Blob Scattering. So far we have considered homogeneous segment density distributions in the brush structures. However, in analogy to semidilute polymer solutions in good solvents, the screening of the excluded volume interaction is expected to produce blob structures[25] which are also at the basis of the theoretical understanding of polymer brushes due to Alexander and de Gennes.

Blob scattering originates from fluctuations of the polymer segment density in the brush. Due to its nature, it relates to disorder and does not lead to interferences with the scattering amplitudes from the average core and brush densities. This disorder scattering can be obtained directly from the excess scattering beyond that expected for homogeneous density distributions.[26] Independent of any model for a two-phase structure homogeneous density distributions require (eqs 3 and 4)

$$S_{\mathrm{bc}}^{2}(Q) = S_{\mathrm{bb}}(Q)S_{\mathrm{cc}}(Q) \tag{22}$$

Thus, the excess brush scattering $I(Q)_{\mathrm{exc}}$ can be formulated as

$$I(Q)_{\mathrm{exc}} = \phi\Delta\rho_{\mathrm{b}}^{2}\left[S_{\mathrm{bb}}(Q) - \frac{S_{\mathrm{bc}}(Q)^{2}}{S_{\mathrm{cc}}(Q)}\right] = \phi\Delta\rho_{b}^{2}\tilde{S}_{\mathrm{bb}}(Q) \tag{23}$$

where S_{bb}, S_{bc}, and S_{cc} are the experimentally obtained partial scattering functions and $\tilde{S}_{\mathrm{bb}}(Q)$ is the partial scattering function for fluctuation scattering. In the simplest case of blob scattering from an ensemble of identical blobs the correlation function for one blob may be described as[27]

$$g(r) \approx r^{1/\nu-3}\exp\left(-\frac{4}{\xi}\right) \tag{24}$$

where ν is the Flory exponent and ξ is the mean blob size. Fourier transformation and normalization leads to

$$I_{\mathrm{exc}}(Q) = \phi\alpha\Delta\rho_{\mathrm{b}}^{2}\,\frac{\sin(\mu\,\arctan(Q\xi))}{Q\xi(1+(Q\xi)^{2})^{\mu/2}} \tag{25}$$

with $\alpha = \nu_{\mathrm{PEP}}m_{\mathrm{s}}(d/L)\xi^{3}(1/\mu)$, where ν_{PEP} is the relative PEP fraction in the diblock copolymer and $\mu = 1/\nu - 1$. Finally, relating ξ with the mean distance between PEP hairs on the PE surface, we get

$$\xi = \left(\frac{2M_{\mathrm{PE}}}{\zeta_{\mathrm{PE}}N_{\mathrm{A}}d}\right)^{1/2} \tag{26}$$

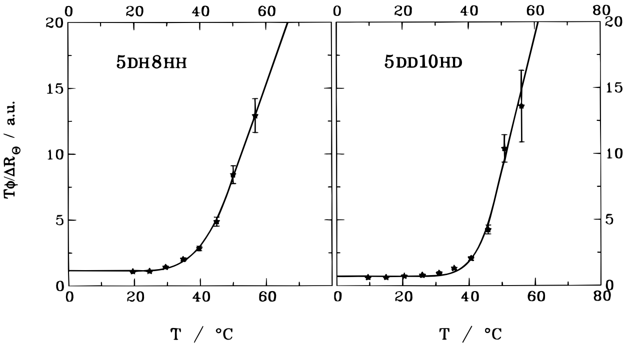

Figure 3. Inverse Rayleigh scattering $T\phi/\Delta R_{\theta}$ from the diblocks 5DH8HH and 5DD10HD resulting from static light scattering at a concentration of 0.005 wt % in decane.

where N_{A} is the Avogadro number and M_{PE} is the molecular weight of the PE block.

4. Experimental Results

4.1. Critical Micellar Concentration (CMC). For a quantitative understanding of the experimental results in terms of the models presented above, it is essential to know the proportion of polymer diblocks which under equilibrium conditions stay in solution. Normally, micellization is driven by the incompatibility of one of the diblock copolymer components with the solvent; e.g., for the PS/PI system in decane for molecular weights above 10^4 the CMC is smaller than 0.001 wt % at room temperature.[28] Here aggregation is caused by the crystallization enthalpy of the PE component. Already long-chain paraffins, though they have the same chemical structure, are hardly soluble in short-chain hydrocarbons; e.g., $C_{36}H_{74}$ can only be dissolved up to 0.5 wt % in decane at room temperature. Thus, diblock copolymers with longer chain PE components are expected to have a very small CMC at room temperature.

In order to investigate the chain solubility, we performed static light scattering measurements on two of the diblock systems measuring the Rayleigh scattering as a function of temperature. Figure 3 presents the temperature dependent inverse Rayleigh scattering for the diblocks 5DH8HH and 5DD10HD. Both at a concentration of 0.005 wt % in decane. Within experimental precision the intensities in both cases have the same temperature dependencies; already above room temperature the intensities saturate, demonstrating that at most only a very minute fraction of the diblocks may stay in solution. Since most of the neutron scattering experiments have been performed at a much higher concentration (2%), for the evaluation of these data any possible small fraction of dilute diblocks can be safely neglected. Toward higher temperature the inverse Rayleigh scattering increases, indicating a gradual dissolution of aggregates. This behavior agrees with the observation that above 70 °C all polymer solutions appear to be clear without any bluish color.

4.2. Morphology of Aggregates—Semiquantitative Results. Below 35 °C an observation of the polymer solutions by phase contrast microscope reveals aggregates of needlelike shapes, extending to several microns. Their thickness, thereby, is within the range of the resolution of the microscope, i.e. 200–500 nm. In order to determine the detailed morphology of these structures, SANS measurements on all samples displayed in Table 1 were performed at a polymer volume fraction of $\Phi = 0.02$ (exception 6HH10DH: $\Phi = 0.01$)

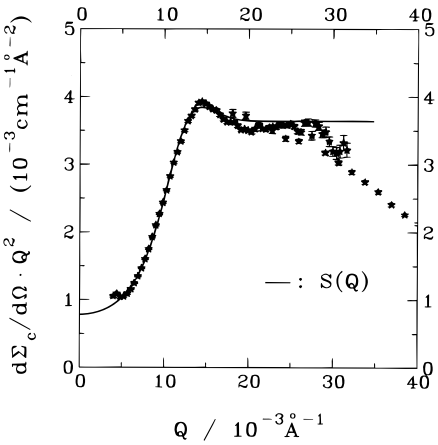

Figure 4. Kratky plot of the partial scattering function under core contrast from 5DH8HH at $\Phi = 2\%$ in decane at room temperature. The solid line displays a fit with the paracrystalline structure factor in the Q range 5×10^{-3} Å^{-1} $\leq Q \leq 25 \times 10^{-3}$ Å^{-1}.

at five different solvent scattering length densities. They were varied in equal steps between the density of fully deuterated decane ($\rho_s = 6.2 \times 10^{10}$ cm^{-2}) and fully protonated decane ($\rho_s = -0.3 \times 10^{10}$ cm^{-2}). With the scattering profiles from these five scattering contrasts the data evaluation proceeded according to procedures outlined in section 2.2 and yielded the partial scattering functions S_{bb}, S_{bc}, and S_{cc}, respectively. Since we deal with very large aggregates, within the experimental accessible Q range ($Q \geq 10^{-3}$ Å^{-1}), the experiments are always performed in the asymptotic high Q limit of eq 13 ($I(Q) \propto 1/Q^2$). Under these circumstances it is appropriate to present the data in terms of a Kratky representation ($I(Q)Q^2$), yielding directly the product of the form factor and the structure factor, e.g., under core contrast this yields

$$\frac{d\Sigma_c}{d\Omega}(Q)Q^2 \approx P_{cc}(Q)S(Q) \tag{27}$$

which is valid for $Q > 2\pi/$R.

Structure Factor. At low $Q < 1/d$ the form factor of a single platelet, governed by its thickness d is about constant. Then eq 27 directly yields the structure factor due to possible stacking of platelets. Figure 4 displays a Kratky plot of the core contrast scattering from 5DH8HH in decane ($\Phi = 0.02$). In the range $5 \times 10^{-3} \leq Q \leq 25 \times 10^{-3}$, the data display the typical profile of a structure factor. The solid line in Figure 4 presents a fit with the paracrystalline structure factor of eq 20. From this fit we find an interplatelet distance of $D = 380$ Å which is accompanied by a large smearing of $\sigma_D = 250$ Å. At the low Q end some tendency for an increasing intensity deviating from the theoretical structure factor for infinite staples is visible, hinting a finite stapling height. For a clear statement, however, the Q range appears to be to small.

Using the D11 SANS instrument at the ILL it was possible to extend the Q range down to $Q \cong 0.8 \times 10^{-3}$ Å^{-1}. Figure 5 displays data, again under core contrast, from the diblock 6HH10DH at $\Phi = 0.02$ in a Kratky representation. The data display again a maximum at $Q = 15 \times 10^{-3}$ Å^{-1}, indicating an interplatelet distance of $D = 400$ Å. Below $Q = 5 \times 10^{-3}$ Å^{-1} an additional strong intensity increase is observed. This intensity increase could be due to two reasons. (i) *Finite platelet dimension*: If Q approaches the inverse platelet dimension R, the Dawson function in a Kratky representation leads to a weak maximum at $QR \cong 3$ with a relative height of about 30%. (ii) *Finite stapling*: The much stronger intensity increase points in the direction of finite aggregates. A fit with eq 21 gives macroaggregates of about eight platelets. The corresponding structure factor is included in Figure 5. The thus computed thickness of 8×40 nm = 320 nm compares well with the "needle" thickness at the border of resolution in the phase contrast microscope.

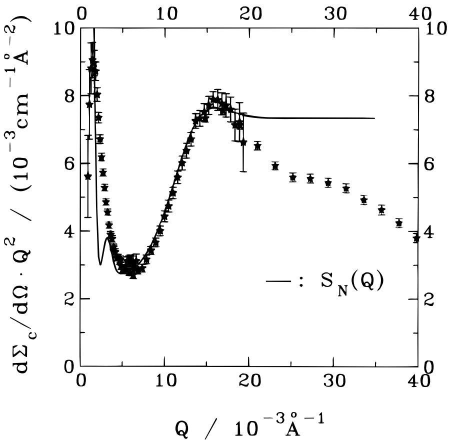

Figure 5. Kratky presentation of the partial scattering function under core contrast from the diblock 6HH10DH at $\Phi = 2\%$ in decane at room temperature. The solid line displays the paracrystalline structure factor for a finite stack with $N = 8$ stacking lamellae. The fit was performed in a Q range 0.8×10^{-3} Å^{-1} $\leq Q \leq 25 \times 10^{-3}$ Å^{-1}.

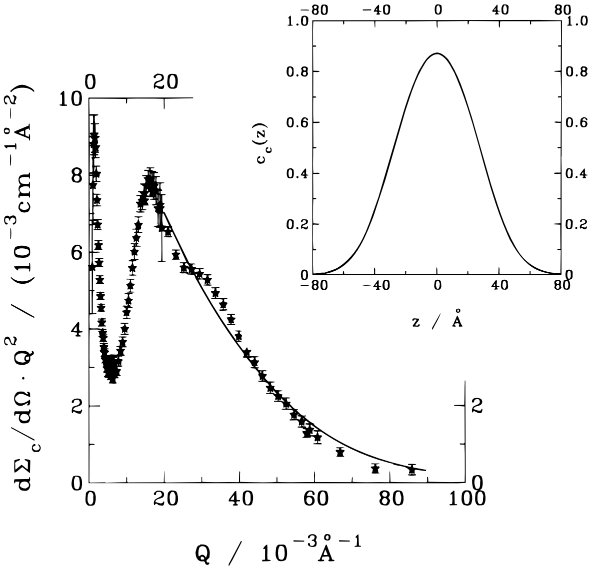

Figure 6. Fit of the core form factor $P_{cc}(Q)$ to the partial scattering function under core contrast from the diblock 6HH10DH at $\Phi = 2\%$ at room temperature ($Q \geq 25 \times 10^{-3}$ Å^{-1}). The insert displays the corresponding density profile of the PE core.

Form Factor of the Polyethylene Core. For $Q \geq 0.02$ Å^{-1} the influence of the interplatelet structure factor becomes small; $S(Q)$ essentially approaches 1. Then according to eq 27 under core contrast the form factor $P_{cc}(Q)$ of the core structure is observed. From eq 16 follows

$$P_c(Q) \approx \left(\frac{\sin(Qd/L)}{(Qd/L)}\right)^2 \exp(-Q^2\sigma_d^{\,2}) \tag{28}$$

Figure 6 displays a fit of the core contrast data from sample 6HH10DH in the Q range above 0.02 $Å^{-1}$ to eq 28, neglecting any interplay between structure and form factor. Such a fit yields a core thickness of $d = 55$ Å. The insert in Figure 6 displays the corresponding density profile in real space. Note the relatively strong smearing resulting from a Gaussian width of $\sigma_d = 18$ Å. This large σ_d value traces back to the relatively strong decrease of the scattering profile toward higher Q. This behavior is typical for all investigated diblock aggregates and not an artifact from overcorrections due to background subtraction.

We wish to note that both the observed structure factors as well as the form factors under core contrast are in good agreement with the postulated morphology of PE platelets forming macroaggregates.

Form Factor of the PEP Brush. Since the length scales governing the interlamellar distances and the brush length are not as well separated as the corresponding lengths in the case of the core, it is more difficult to access the brush form factor in a semiquantitative way. Furthermore, in the case of the brush beyond the average density profiles, also concentration fluctuations are important. From eqs 15–17 and 25 the macroscopic cross section for brush scattering in the Kratky representation becomes

$$\frac{d\Sigma}{d\Omega}(Q)Q^2 \approx P_{bb}(Q)S(Q) + I_{ex}(Q)Q^2 \qquad (29)$$

Thereby, P_{bb} represents the from factor of the homogeneous average brush profile while I_{ex} results from the concentration fluctuations in the brush (blob scattering becoming important for Q values beyond 0.05 $Å^{-1}$). With the structure factors determined from the results under core contrast, the experimental data were fitted with parabolic and smeared step function profiles eqs 16 and 17. Figure 7 displays experimental partial scattering functions for brush contrast from the diblocks 5DH8HH and 6HH10DH in a Kratky presentation. Compared to the core contrast, the data of the profiles are more rich in structure and display two different regimes. At low Q as a result of the interplay between $S(Q)$ and the form factor, a first peak appears around $Q \approx 10 \times 10^{-3}$ $Å^{-1}$. This peak is followed by a deep minimum in the neighborhood of $Q = 0.02$ $Å^{-1}$. This pronounced minimum is caused by interference effects from the scattering of the two brushes on both sides of the PE core. Its position is a measure of the distance S between the center of masses of the two brushes, $S \approx \pi/Q \approx 160$ Å.

The full (Gaussian profile) and dashed (parabolic profile) lines in Figure 7 represent the fit of these two profiles to the experimental results. In both cases the experimental data can be well described except for deviations occurring at higher Q. While in the case of the 5DH8HH diblock both profiles lead to an equivalent description for the 6HH10DH system, the smeared step function profile appears to be favored. The inserts compare the respective density profiles in real space.

Internal Brush Structures. According to section 3.3 the brush scattering can be understood as a superposition of the scattering from the average density profile of the brush yielding $P_{bb}(Q)$ and scattering originating from the concentration fluctuation within the brush (eq 25). This disorder type scattering can be derived without model assumptions from the partial scattering functions according to eq 23. Figure 8 displays the partial scattering function for brush contrast $S_{bb}(Q)$ (eq 5) and for fluctuation scattering $\tilde{S}_{bb} = S_{bb} - S_{bc}^2/S_{cc}$ for the 5DH8HH diblock system at $\Phi = 2\%$. Obviously, for Q values exceeding 0.05 $Å^{-1}$ the total

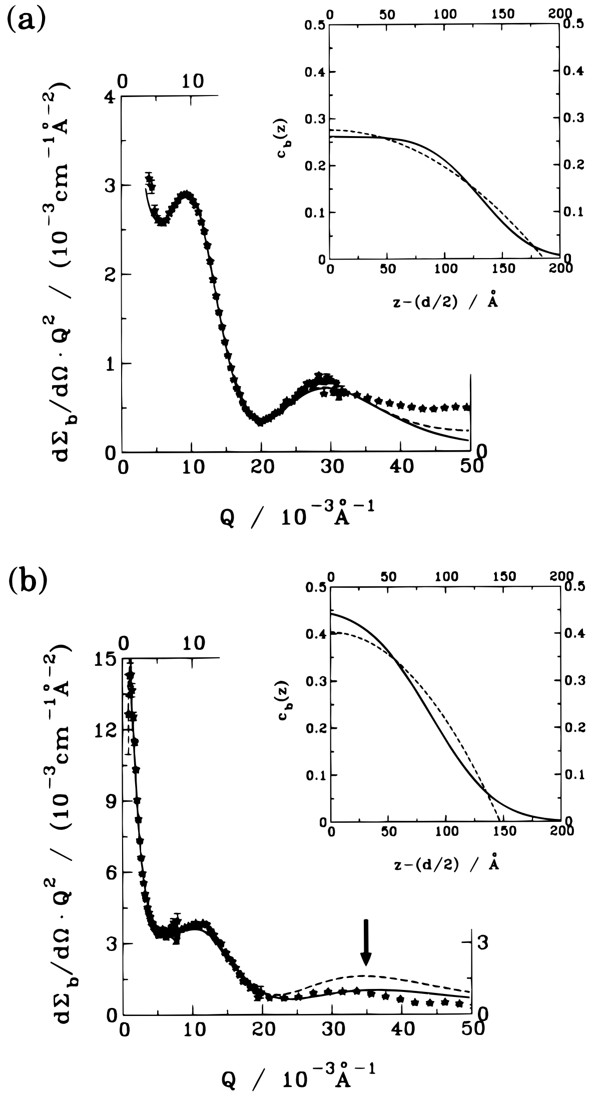

Figure 7. Kratky representation of the partial scattering function under brush contrast for the diblocks (a) 5DH8HH and (b) 6HH10DH each at $\Phi = 2\%$ at room temperature. The solid and dashed lines display fits with $P_{bb}(Q) \times S(Q)$ using different brush profiles. The inserts display the corresponding polymer densities in real space (solid line, smeared step function; dashed line, parabolic profile).

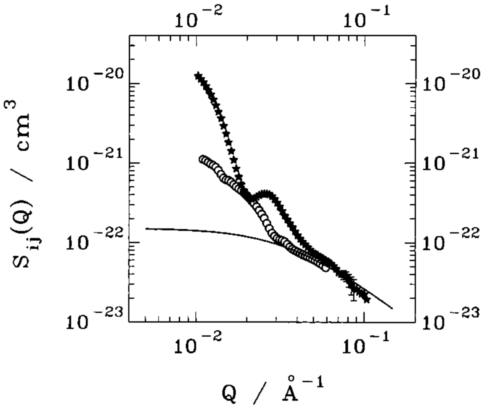

Figure 8. Partial scattering function for brush scattering $S_{bb}(Q)$ (★) and fluctuation scattering $\tilde{S}_{bb}(Q)$ (○) for the diblock 5DH8HH at $\Phi = 2\%$ and room temperature. The solid line displays a fit with the expression for blob scattering (eq 25) to this fluctuation scattering.

scattering from the brush coincides with the fluctuation scattering. Thus, in this Q regime the observed cross section is dominated by blob scattering. In this range a fit with the expression for blob scattering (eq 25) may be used to estimate the blob size, yielding $\xi \approx 30$ Å. We emphasize, however, that due to the interplay between the different scattering contributions this estimation of ξ is not very accurate. As we shall see below from combined fits of all data, smaller values for ξ evolve. Toward smaller Q additional disorder scattering not accounted for by the blob picture appears. Its origin is presently not known but may be related, for example, to lateral disorder. Also recent neutron spin echo experiments on the brush dynamics[29,30] have identified an elastic frozen component superimposing the quasielastic scattering from relaxation processes within the polymer brush which relates directly to this excess fluctuation scattering.

4.3. Quantitative Results from Contrast Variation. Figure 9 displays the scattering profiles which have been obtained from the diblock 5DH8HH at $\Phi = 0.02$ at the five different decane contrasts. In order to emphasize the prevailing features, in the preceding section we tried in a semiquantitative way to evaluate the different characteristics of the scattering patterns. Here we present a quantitative fit of all available data by common variation of parameters. We also consider explicitly the Q resolution of the different small angle scattering machines employed by convoluting the theoretical scattering functions with the calculated respective resolutions before comparing with the data. The fitting procedure was based on the following variable parameters

d	PE core thickness
σ_d	Gaussian smearing of the core profile
L, L_p	height of the step function-like or parabolic PEP brush, respectively
σ_L	Gaussian smearing of the steplike PEP brush
D	interlamellar distance in the macroaggregates
σ_D	Gaussian smearing of the stacking period
N	number of lamellar aggregates in macroaggregates
ξ	average blob size in the brush
α	intensity factor for blob scattering, this factor was used in order to account for the total disorder scattering incorporating eq 25 into the cross section

For practical purposes the lateral dimension R was fixed to 1500 Å, a value which does not affect the profiles in the visible Q range.

In the fit, the determination of the brush parameters L or L_p and σ_L as well as the structure factor parameters D, σ_D, and N was achieved in an unambiguous way—the scattering profiles relating to these parameters are rich in structure and are very sensitive to the variation of parameters. On the other hand, an access to the core parameters d and σ_d turned out to be considerably more difficult. The core form factor presents itself as a rather featureless scattering profile without exhibiting any particular structure. Under these circumstances the value for the core thickness depends strongly on the correct absolute normalization of the data which in turn relies on the precise knowledge of the corresponding scattering length densities. For a correct determination of the core thickness d the availability of similar diblocks with different labeling was very helpful. All fits were performed using alternatively the smeared step function or the parabolic profile, respectively for the brush. The solid lines in Figure 9a display the obtained result for the smeared step function brush profile while those in Figure 9b represent the result for the parabolic shape. Tables 3−6 summarize the resulting parameters obtained for the different diblock systems.

First we like to emphasize that obviously the model of a lamellar PE structure surrounded by a polymer brush forming macroaggregates describes the experimental scattering profiles in a very satisfactory way.

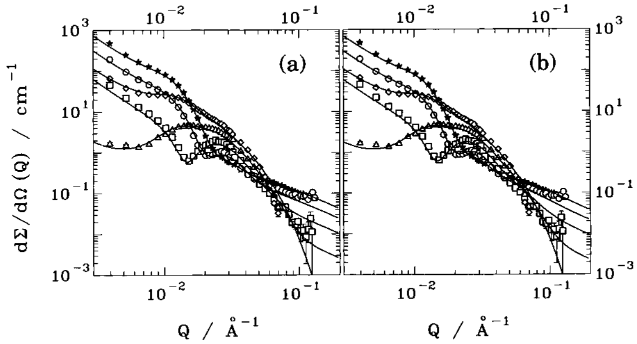

Figure 9. Data profiles obtained from contrast variation using five different decane contrasts for the diblock 5DH8HH at $\Phi = 2\%$ and room temperature. The solid lines display the fit prediction using (a) a smeared step function and (b) a parabolic brush profile. The scattering lengths densities of decane corresponding to the different curves are (★) 6.2×10^{10} cm^{-2}, (○) 4.6×10^{10} cm^{-2}, (□) 2.9×10^{10} cm^{-2}, (△) 1.3×10^{10} cm^{-2}, and (◇) -0.31×10^{10} cm^{-2}. For better visibility only every third data point is displayed.

Table 3. Core Parameters from the Combined Fits (d, core thickness; σ_D, Smearing Parameters) Assuming Smeared Step Function or Parabolic Brush Profiles, Respectively (Errors from Statistical Analysis Only)

	smeared step function		parabolic profile	
diblock	d/Å	σ_d/Å	d/Å	σ_d/Å
5DH8HH (2%)	38 ± 3	21 ± 3	37 ± 3	21 ± 3
5DD10HD (1%)	32 ± 4	16 ± 3	32 ± 4	16 ± 3
6HH10DH (1%)	52 ± 4	17 ± 2	52 ± 4	16 ± 2
6HH10DH (2%)	52 ± 4	17 ± 2	52 ± 4	17 ± 2
10DH16HH (2%)	80 ± 4	6 ± 1	80 ± 4	5 ± 1
6HH15DH (2%)	44 ± 4	23 ± 3	40 ± 4	23 ± 3
6DH20HH (2%)	32 ± 2	15 ± 2	30 ± 1	15 ± 2

Table 4. Brush Parameters from the Combined Fits Assuming Smeared Step Function (L, Length; σ_L, Smearing) or Parabolic (L_p, Length) Profiles, Respectively[a]

	smeared step function		parabolic profile
diblock	L/Å	σ_L/Å	L_p/Å
5DH8HH (2%)	123 ± 2	42 ± 2	183 ± 2
5DD10HD (1%)	124 ± 3	67 ± 3	190 ± 3
6HH10DH (1%)	103 ± 3	48 ± 3	167 ± 2
6HH10DH (2%)	93 ± 5	46 ± 4	155 ± 2
10DH16HH (2%)	225 ± 2	81 ± 2	334 ± 2
6HH15DH (2%)	186 ± 7	96 ± 7	303 ± 3
6DH20HH (2%)	231 ± 5	72 ± 5	333 ± 4

[a] L_p should be compared to $L + \sigma_L$ (errors are statistical).

Table 5. Structure Factor Parameters from the Combined Fits (Repetition Distance, *D*; Smearing, σ_D; Number of Platelets in the Macroaggregate, *N*) Assuming Smeared Step Function or Parabolic Brush Profiles, Respectively (Errors from Statistical Analysis)

	smeared step function			parabolic profile		
diblock	D/Å	σ_D/Å	N	D/Å	σ_D/Å	N
5DH8HH (2%)	404 ± 5	245 ± 2	∞	414 ± 6	249 ± 2	∞
5DD10HD (1%)	496 ± 10	253 ± 7	16 ± 4	500 ± 10	253 ± 7	16 ± 4
6HH10DH (1%)	365 ± 7	233 ± 3	16 ± 4	367 ± 9	233 ± 3	16 ± 4
6HH10DH (2%)	362 ± 5	227 ± 4	24 ± 4	365 ± 5	228 ± 4	24 ± 4
10DH16HH (2%)	842 ± 12	424 ± 10	∞	834 ± 12	424 ± 9	∞
6HH15DH (2%)	690 ± 8	442 ± 10	24 ± 4	680 ± 10	485 ± 11	24 ± 4
6DH20HH (2%)	1043 ± 10	567 ± 8	24 ± 4	1040 ± 10	570 ± 7	24 ± 4

Table 6. Blob Parameters (Blob Size ξ Intensity Parameter α; See Eq 25) from the Combined Fit Assuming Smeared Step Function or Parabolic Brush Profiles, Respectively (Statistical Errors Only)

	smeared step function		parabolic profile	
diblock	ξ/Å	α/Å^3	ξ/Å	α/Å^3
5DH8HH (2%)	22 ± 2	7300 ± 650	20 ± 2	5400 ± 600
5DH10HD (1%)	25 ± 5	5000 ± 1000	25 ± 5	3500 ± 1000
6HH10DH (1%)	20 ± 2	6100 ± 2200	20 ± 2	4500 ± 2000
6HH10DH (2%)	20 ± 2	4100 ± 1000	20 ± 2	2500 ± 1000
10DH16HH (2%)	19 ± 3	4500 ± 500	19 ± 3	4000 ± 500
6HH15DH (2%)	16 ± 4	2600 ± 1000	16 ± 4	2000 ± 1000
6DH20HH (2%)	16 ± 4	4500 ± 900	15 ± 3	4000 ± 900

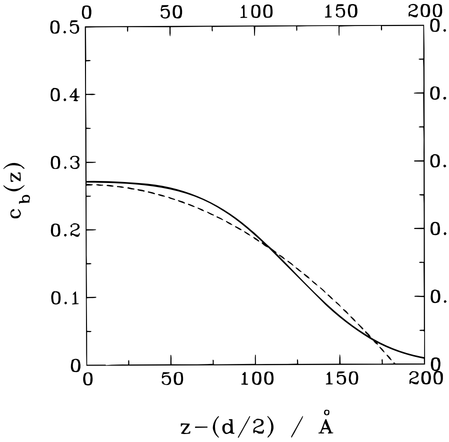

Figure 10. Comparison between the smeared step function and parabolic brush profiles for the diblock 5DH8HH at Φ = 2% and room temperature.

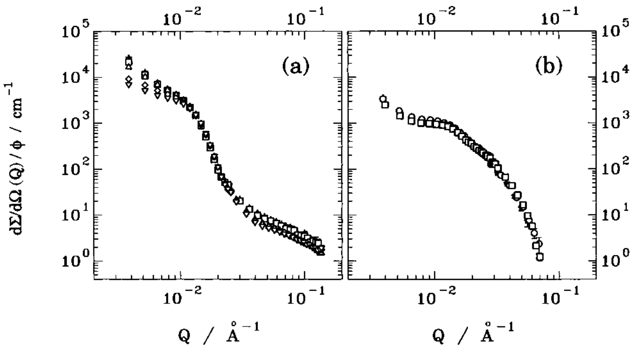

Figure 11. Concentration-dependent scattering profiles from the diblock 5DH8HH at room temperature under (a) brush and (b) core contrast: Φ = 0.5% (★), 1% (○), 2% (□), 5% (△), 8% (◇), and 10% (▽). For better visibility only every third data point is shown.

Table 7. Concentration-Dependent Structure Factor Parameters for the Diblock 5DH8HH (Repetition Distance, *D*; Smearing, σ_D; Number of Platelets in Macroaggregate, *N*) Assuming Smeared Step Function or Parabolic Brush Profiles, Respectively (Φ, Polymer Volume Fraction) (Statistical Errors Only)

	smeared step function			parabolic profile		
Φ/%	D/Å	σ_D/Å	N	D/Å	σ_D/Å	N
0.5	440 ± 4	263 ± 2	8 ± 2	437 ± 4	261 ± 2	8 ± 2
1	440 ± 7	253 ± 3	16 ± 2	439 ± 7	253 ± 3	16 ± 2
2	395 ± 5	243 ± 3	∞	397 ± 5	243 ± 3	∞
5	437 ± 4	271 ± 1	∞	446 ± 6	271 ± 2	∞
8	456 ± 4	232 ± 1	∞	465 ± 5	231 ± 2	∞
10	463 ± 3	207 ± 1	∞	473 ± 4	205 ± 2	∞

We would like to mention that for an overall accurate picture it is essential to perform measurements at different solvent contrasts. Taking only one of these contrasts, as one would do, for example, in an X-ray experiment, an accurate unique determination of the parameter set is impossible.

Though the form factor parameters of a single lamellar structure and the structure factor parameters have been determined independently, in all cases the relation $2L_p + d = D \pm \sigma_D$ holds. Thus, the stacking period *D* coincides with the lateral aggregate size. At a first glance also the very thin core thicknesses of $d \cong 50$ Å are astonishing—they are considerably smaller than what is found in melt grown polyethylene crystals where the long period is hardly smaller than 100 Å. We will come back to this feature in the next section.

Finally, we draw attention to the verification of the parabolic brush profile proposed by Milner et al. Figure 10 displays the comparison of the fitted parabolic and smeared Gaussian profiles for the case of the 5DH8HH diblock system as obtained from the joint fit. With the smeared step function the fitting procedure had the freedom to vary the shape of the brush density significantly; the obtained profile resembles very closely the parabola one gets from a forced fit. Similar agreement was also obtained for all other systems.

4.4. Concentration Effects. Taking 5DH8HH as a representative diblock, we investigated the concentration-dependent scattering profiles over large concentration range 0.5% ≤ Φ ≤ 10%. Figure 11 presents scattering profiles obtained under core and brush contrast, respectively. The scattering patterns are normalized to concentration in order to make them comparable. While in the intermediate *Q* range all data sets collapse to a single curve, in particular at lower *Q* and higher concentrations, we realize a systematic intensity decrease with increasing concentration hinting at a more pronounced structure factor at higher polymer volume fraction. The data were evaluated in terms of the aggregating platelet model by employing the Gaussian smeared step function profile for the brush. Table 7 presents the obtained concentration-dependent parameters. Figure 12 visualizes the results in terms of the structure factor calculated on the basis of the parameters displayed in Table 7. Two features are evident: (i) At low *Q* and small Φ a strong intensity increase evolves from the finite size of the macroaggre-

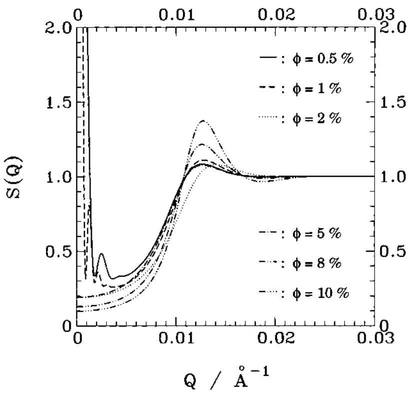

Figure 12. Results for the concentration-dependent structure factors for the diblock 5DH8HH at room temperature.

gates. With increasing concentration this extra low Q scattering disappears, indicating larger lamellar stacks. (ii) This increase of stacking is accompanied by a more pronounced first maximum of $S(Q)$ appearing at higher Φ. Thus, while the size of the macroaggregates grows with increasing concentration, its structure becomes more organized.

4.5. Micellar Orientation under Shear. Shear experiments in colloidal and polymer physics are often used in order to induce ordering phenomena or to orient already locally ordered structures.[31−33] In this chapter we present shear experiments on the diblock system 6HH15DH at a polymer volume fraction of $\Phi = 10\%$, revealing information on the organization of the platelets within the macroaggregates.

The experiments were started using the Couette cell at the small angle neutron scattering instrument in Risø. The cell provided a 0.5 mm slit allowing for a maximum shear rate of $\dot{\gamma}_{\max} = 967\ \text{s}^{-1}$. At $\Phi = 10\%$ the sample exhibits a gel-like viscosity. Filling the sample into the cell leads, as expected, to an isotropic scattering pattern. Introduction of the rotor into the Couette cell from above changes the scattering pattern to two peaks appearing in the scattering plane. Obviously, under these conditions the lamellar platelets are oriented perpendicular to the horizontal plane. Turning the rotor exerting shear in the horizontal direction with the shear gradient in the direction of the neutron beam causes the scattering pattern to turn by 90°. Now the Bragg spots appear above and below the horizontal scattering plane. This pattern remains stable up to $\dot{\gamma} = 500\ \text{s}^{-1}$. Above this shear rate the scattering becomes isotropic. A subsequent reduction of $\dot{\gamma}$ does not bring back the former pattern. Obviously, by the high shear rate the lamellar structures are destroyed and do not reassemble. Only heating above the melting temperature (70 °C) and subsequent cooling reproduces the original phenomena. The observation of Bragg spots below and above the horizontal plane requires that the lamellar plane giving rise to these reflections and the horizontal plane must coincide. At a first glance this observation is counter-intuitive: a platelet surface in the direction of the shear gradient should be unstable compared to a perpendicular orientation.

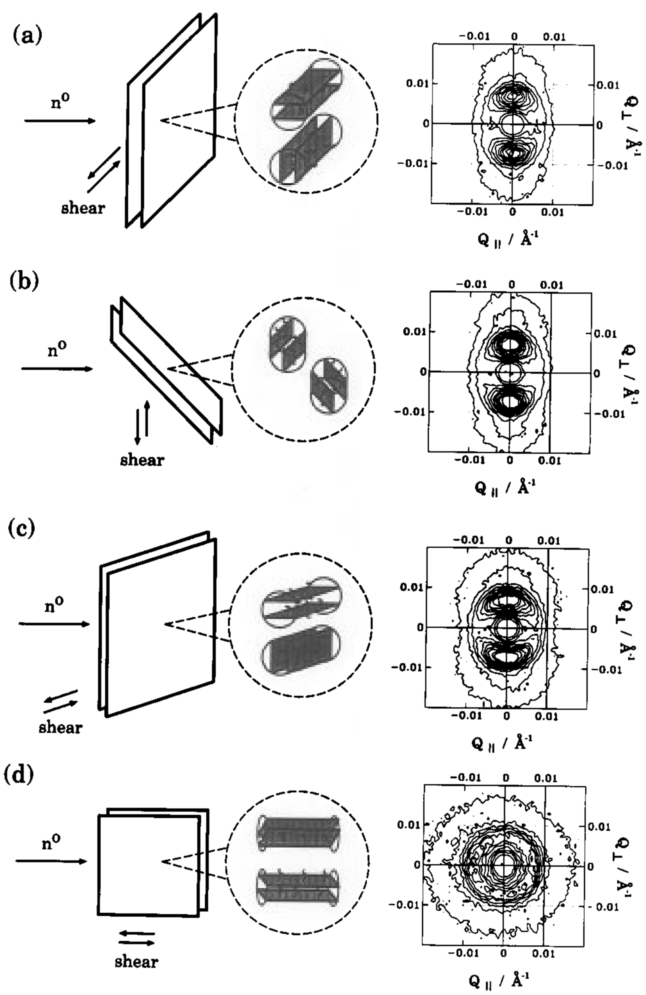

Figure 13. Shear experiments. The figures display schematically the scattering geometry, the shear direction, and the tilt of the sample which stays between two thin quartz plates; the obtained scattering patterns are displayed on the right side of the figures, and the inserts in the middle visualize the platelet organization within the needlelike macroaggregates. (a) Perpendicular geometry: neutron beam direction and shear direction are perpendicular. (b) Sample is turned by 45° around an axis parallel to the shear direction. (c) Sample is turned around an axis perpendicular to the shear direction by 45°. (d) Sample is turned by 85° around an axis perpendicular to the shear direction. All experiments were performed on the diblock 6HH15DH at $\Phi = 10\%$ and room temperature under core contrast.

The Couette cell does not allow alterations in the shear geometry relative to the neutron beam direction. Since the observed pattern remains stable even after removal of the shear gradient, the gel-like sample in a second set of experiments was brought between two thin quartz plates which were sheared by hand relative to each other. Afterward they were oriented in different ways relative to the incoming neutron beam. Parts a−d of Figure 13 display the qualitative changes of the two-dimensional scattering patterns, when the sample is turned around an axis parallel or perpendicular to the shear direction. Figure 13a presents a geometry equivalent to that of the Couette cell, revealing an identical scattering pattern with spots above and below the horizontal plane. Figure 13b shows the pattern arising if the sample is turned around an axis parallel to the shear direction by an angle of 45°. Under these circumstances no change compared to the outgoing situation of Figure 13a is observed. In Figure 13c,d the effects of turning around an axis perpendicular to the shear are displayed. Turning around 45° already smears out the pattern considerably (Figure 13c). Increasing this angle to 85° finally reveals an isotropic pattern.

These qualitative observations allow a clarification of the way the PE lamellae assemble within the macroaggregates. The corresponding structures are shown in the inserts. As was mentioned above, from observations by the phase contrast microscope, the macroaggregates have needlelike shapes. Within these needles the planes of the PE lamellae must orient parallel to the long direction of the needles—the needles themselves orient with their long direction parallel to the shear. Thereby the surfaces normal to the PE planes are oriented in a random fashion perpendicular to the needle direction. In this picture the shear results are explained naturally. Turning around an axis parallel to the shear direction does not change anything. Out of the ensemble of PE planes there is always a fraction with an orientation fulfilling the Bragg condition. Those planes give rise to the reflexes above and below the scattering plane. The situation changes if one turns around an axis perpendicular to the shear, when more and more planes are brought into the Bragg condition. At 85° basically all planes whatever their orientation within the needle may give rise to Bragg scattering and produce a Debye–Scherrer ring.

In summary, the experiments on the aggregation of PE–PEP diblock copolmers in decane revealed a hierarchy of structures. The PE component forms lamellar crystals with PEP hairs on the outside. These hairs form a brush with an average density profile close to a parabolic shape. The spatial extension of these aggregates in the direction of the lamella is larger than the experimental range of SANS and can directly be observed with a light microscope. The platelets stack together to form macroaggregates. At low polymer volume fraction these structures are loosely organized and contain about eight platelets. Increasing organization and macroaggregation is observed with increasing polymer volume fraction. The interlamellar distances thereby correspond rather well to the lateral size of a single aggregate. Macroscopically, the macroaggregates have the form of needles with a length of about 5 μm. Within these needles the platelet planes are extending in the long direction of the needle.

5. Discussion

5.1. Thermodynamics of Platelet Formation. In the following we briefly introduce the brush model of Alexander[21] and de Gennes,[22] derive a number of scaling relations and in a first step compare the experimental parameters with these scaling predictions. In a second step we go further and try to assess quantitatively the different contributions to the free energy.[34] This will force us to consider explicitly the defect structure resulting from the ethyl side branches in the PE synthesized from hydrogenating anionically polymerized polybutadiene.

The Alexander–de Gennes brush model is derived from an analogy to semidilute polymer solutions. There, the screening of the excluded volume interaction leads to a blob structure with swollen chain sections inside the blobs.[25] Size ξ and segment number g within the blobs are related by the scaling relation for chains in good solvents

$$\xi \approx g^{\nu} \tag{30}$$

$\nu = {}^3/_5$ thereby is the Flory exponent. While for homogeneous semidilute polymer solutions ξ only depends on the average polymer concentration, for a brush ξ relates to the number of hairs evolving from the tethering surface per unit surface area. With Ω being the hair surface density we have

$$\xi \cong \Omega^{-1/2} \tag{31}$$

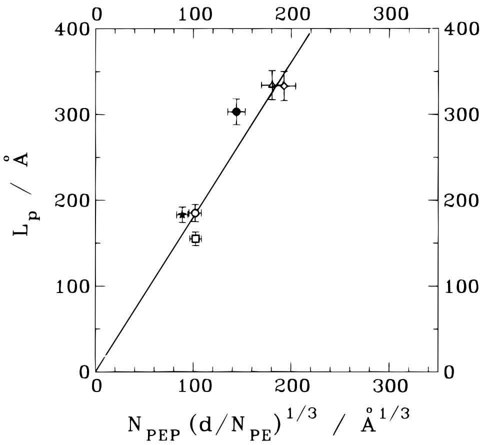

Figure 14. Scaling of the brush length L_p with the number of monomers within the respective diblock copolymer and the PE core thickness for $\Phi = 2\%$ and room temperature: 5DH8HH (★); 5DD10HD (○); 6HH10DH (□); 10DH16HH (△); 6HH15DH (●); 6DH20HH (◇).

The brush then evolves as a string of blobs. The brush length L_p follows from the condition that the segment density within one blob should be equal to the average density within the brush. (This relation requires the simple assumption of a rectangular brush profile; however, the actual parabolic profile does not change the scaling results.)

$$\frac{g}{\xi^3} = \frac{N_{PEP}}{L_p \xi^2} \tag{32}$$

With eqs 26, 30, and 31 we finally arrive at a first scaling relation for the brush length L_p

$$L_p \approx N_{PEP}\Omega^{1/3} \approx N_{PEP}\left(\frac{d}{N_{PE}}\right)^{1/3} \tag{33}$$

Since all quantities in eq 33 are known from experiment (Tables 1 and 3–6), this scaling relation can be tested on the basis of our results. Figure 14 displays L_p as a function of $N_{PEP}(d/N_{PE})^{1/3}$. The error bars relate to estimated systematic errors as $\Delta d/d \approx 10\%$, $\Delta L_p/L_p \approx 5\%$, and $\Delta N_{PEP}/N_{PEP} \approx 5\%$. The experimental points follow with good accuracy a line through the origin and thus support the scaling relation of eq 33.

Further scaling relations may be obtained from a consideration of the free energy F of the aggregate.[1] Two contributions prevail: (i) The chain stretching within the brush leads to a loss of chain conformational entropy. It can be estimated by the number of blobs n_b per chain within the brush times k_BT

$$F_{PEP} \approx k_B T n_b = k_B T \frac{L}{\xi} = k_B T N_{PEP} \Omega^{5/6} \tag{34}$$

From the polyethylene crystalline lamella we get an enthalpic contribution to the free energy relating to the enthalpy loss as a consequence of chain folding. There, the free energy per chain is just given by the number of folds per chain times the folding energy E_f

$$F_{PE} = E_f n_f = E_f \frac{lN_{PE}}{d} \approx \Omega^{-1} \tag{35}$$

Equations 34 and 35 show that both contributions to

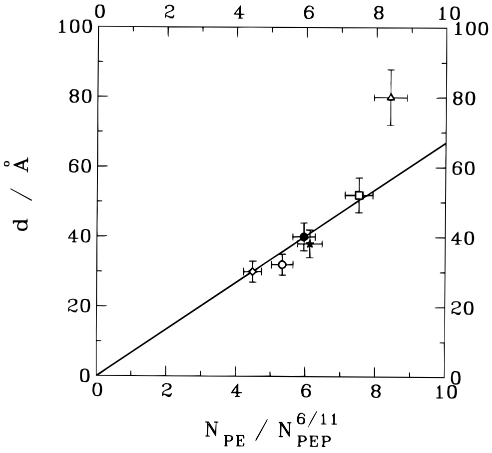

Figure 15. Scaling of the core thickness of the lamellar aggregates with the monomer number of the corresponding diblock copolymers, each at $\Phi = 2\%$ and room temperature: 5DH8HH (★); 5DD10HD (○); 6HH10DH (□); 10DH16HH (△); 6HH15DH (●); 6DH20HH (◇).

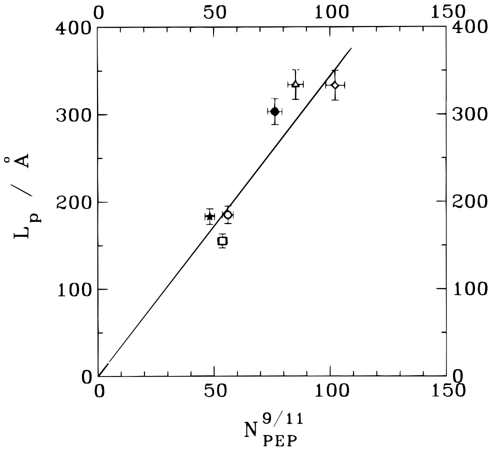

Figure 16. Scaling of the brush length L_p with the monomer number of the corresponding brush hair for $\Phi = 2\%$ and room temperature: 5DH8HH (★); 5DD10HD (○); 6HH10DH (□); 10DH16HH (△); 6HH15DH (●); 6DH20HH (◇).

the free energy can be written as a function of the hair surface density Ω

$$F = F_{PEP} + F_{PE} = c_1\Omega^{-1} + c_2\Omega^{5/6} \qquad (36)$$

Minimization of the total free energy with respect to Ω leads to a number of further scaling relations

$$\Omega \approx N_{PEP}{}^{-6/11}$$

$$d = N_{PE}N_{PEP}{}^{-6/11} \qquad (37)$$

$$L_p \approx N_{PEP}{}^{9/11}$$

The second and third relation again may be tested on the basis of our data. Figures 15 and 16 display the results. Therein the experimental errors have been estimated as before. Again both graphs show a reasonable agreement with the proposed scaling laws.

From the above model considerations core and brush thickness adjust themselves from a balance between the entropy loss in the stretched brush and the enthalpy costs of folding the polyethylene chains. In the following we would like to quantify the different contributions to the free energy using the diblock 5DH8HH as an example. In this system the PE block contains about 325 CH_2 groups leading to a stretched length of about 430 Å. Taking the experimental core thickness of d = 38 Å, we arrive at about 11 folds per polyethylene chain. Using E_f = 170 meV[35] as a typical fold energy, the enthalpy contribution to the free energy becomes F_{PE} = 1.9 eV.

In order to calculate the free energy of the brush, we have to estimate the number of blobs in the brush. Using eq 26 a blob size of 21 Å is found. With the brush length of L_p = 123 Å for this block copolymer system according to eq 34 we obtain six blobs per PEP chain, leading to an entropy contribution to the free energy of F_{PEP} = 0.15 eV.

Comparing the core and brush contribution, we realize that in the frame of our approach the system is grossly unbalanced; e.g., with an increase of the core thickness, folds could be spared with little increase of the entropic contribution from the brush. Thus, there must be other contributions to the free energy which explain the observed structures. One could think about a contribution from the disorder entropy relating to the distribution of hairs at the surface. Following a simple free gaslike approach, however, this contributes only about k_BT per PEP chain. The large energy contribution needed, in order to counterbalance the fold energy, most likely arrives from the same source, namely trans—gauche energy differences of the PE chain.

The way the PE components have been synthesized leads to about 18 ethyl side branches per 1000 methylene groups in the PEP chain. These ethyl branches, if incorporated into the PE crystal, cause high defect energies. Recently, Gaucher and Séguéla[17] have investigated the change in melting enthalpy ΔH_f of polyethylene crystals as a function of the total ethyl group concentration. For our case they arrive at ΔH_f = 75 J g^{-1}, yielding a defect energy of $E^{def} \approx$ 600 meV. In their study they found a strong tendency to expel ethylene side branches into the amorphous phase. Such a mechanism may also be regarded at the origin of our observation of seemingly too thin PE crystals. With the low number of ethyl branches realized in our PE chains the Poisson distribution of side groups is very close to an equal distribution, yielding a rather uniform probability of p = 0.018 to find an ethyl branch at any CH_2 group. With an increase of the PE surface the probability to bring an ethyl side branch in the neighborhood of this surface increases. In the neighborhood of the surface we can assume that the energy costs to incorporate the ethyl branch into the crystal is strongly diminished. In the folding region these energy costs will be minimal. In this spirit we may formulate an expression for the defect contribution to the free energy

$$F_{def} = F^0_{def} - n_f n_s p E_{def} \qquad (38)$$

Thereby, F^0_{def} is the defect energy for the incorporation of all ethyl groups into a large PE crystal, n_s gives the number of methylene positions in the neighborhood of the fold at which the energy costs for the incorporation of an ethyl group are strongly reduced. The product $n_f n_s p$ is then the number of ethyl branches which are not contributing to the defect energy. We note that F_{def} as F_{PE} scales with Ω^{-1}. Thus, the scaling properties of the total free energy are not affected by the addition of this defect term—the results for the scaling relations (eq 37) thus remain. In our example the PE chain contains on the average about 6 ethyl side branches. In order to equilibrate the free energy three of them have to be

Table 8. Parameters Involved in the Calculation of the van der Waals Interaction between Two Platelets

quantity	symbol	value	source
length (platelet)	L_s	5 μm	optical microscopy
width (platelet)	W	500 nm	optical microscopy, SANS (D11)
area (platelet)	A	2.5×10^{-12} m^2	see above
PE-core thickness	d	5 nm	SANS
brush width	L_p	25 nm	SANS
brush volume frac	Φ_b	0.3	stoichiometry
refractive index (PE)	n_{PE}	1.53	38
refractive index (decane)	n_d	1.41	CRC Handbook
dn/dc (PEP in decane)	$(dn/dc)_{PEP}$	7.945×10^{-2}/(g/mL)$^{-1}$	own measurement
main absorption (PE)	ω_{PE}	1.3×10^{16} s^{-1}	39
main absorption (PEP)	ω_{PEP}	1.3×10^{16} s^{-1}	estimated
main absorption (decane)	ω_d	1.45×10^{16} s^{-1}	39

close to the surface. From this requirement $n_s \approx 15$ follows from eq 38. Thus for each fold ethyl branches at a total number of 15 methylene positions do not contribute to the deformation enthalpy. Such a relatively large number of affected methylene groups must mean a rather rough surface structure. This conjecture is also supported by the large smearing parameters σ_d found for the PE core (Table 3).

To summarize, the thermodynamics of aggregation for the PE−PEP diblocks is governed by a delicate balance between the polyethylene folding enthalpy and the defect energies associated with the incorporation of ethyl branches on the one hand and the entropy loss due to stretching of the PEP chains in the brush on the other hand. Considering the independently obtained experimental data on folding and defect energies, a quantitative understanding of the aggregate sizes becomes possible. We note that a PE−PEP diblock, where the PE component would be strictly linear, would form much thicker lamellae.

5.2. Macroaggregation by van der Waals Forces. As has been pointed out earlier, even a weak interaction may lead to the stacking of extended platelets if the contact area is large. The translational entropy of a platelet scales with the logarithm of its mass M, whereas any contact type interaction that is proportional to the contact area scales with M provided the platelets have a constant thickness. Consequently, above a certain threshold mass even a tiny attraction interaction will win and lead to aggregation. At short distances, of course, the brushes on the platelets will repel each other due to entropy reduction (osmotic pressure) if two brushes try to interpenetrate. However, as soon as the mutual distance exceeds the extension of the brushes, this repulsion goes to zero and only long range electrostatic forces remain. From those forces only the attractive van der Waals (vdW) force is expected to contribute to the interaction of the platelets. Only if the vdW interaction energy at "contact" of two opposite brushes is large enough, will aggregation occur.

Here we provide a semiquantitative estimation of the associated energy and entropy using the "average" aggregate parameters listed in Table 8. The brush profile has been assumed as parabolic, a shape supported by our experiments and predicted theoretically.

To compute the vdW interaction, the expression of Parsegian and Ninham[36] for layered assemblies of infinite slabs has been used. This formulation is an extension of the Lifshitz result for two semi-infinite media and accounts for any retardation, nonadditivity, and temperature effects. The parabolic brush density profile has been entered as a discrete series of slabs with varying PEP density, e.g., the parabolic density profile has been replaced by a stepwise constant approximation. One brush has been modeled by 12−26 slabs. In addition to the slab widths the interaction depends on the dielectric functions of the media in the slabs ($i = 1, ..., N$) at imaginary frequency arguments, $\epsilon_i(i\zeta)$. The simplest model beyond a constant emerges from a simple oscillator model[37]

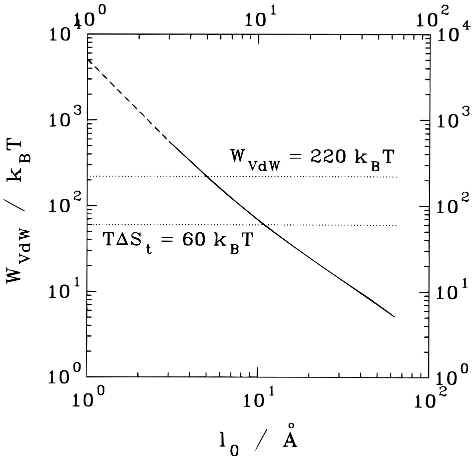

Figure 17. Magnitude of the van der Waals interaction in units of k_BT between two planar PEP brushes as a function of distance l_0 calculated for $T = 300$ K in decane (see text). The two horizontal lines give the threshold for the translational entropy and the value for the van der Waals energy at close contact ($l_0 = 5$ Å).

$$\epsilon_i(i\zeta) = 1 + \frac{f_i}{1 + (\zeta/\omega_i)^2} \qquad (39)$$

The ω_i values are taken from Table 8, and the f_i values for substance i follow from the requirement to reproduce the index of refraction or the corresponding substances, respectively. For the brush consisting layer by layer of a mixture of PEP and decane, the ϵ values are linearly combined according to the volume fraction. The free energy due to vdW interaction has been computed using eqs 12−15 of ref 36. The model consisted of two PE-core slabs each with one modeled brush on the contact side. The resulting energy values are to be understood as differences between the chosen near contact situation and the case of infinite distance of the two PE-brush layers, all the intermediate being filled with decane. The nested summation and integration of eq 12 of ref 36 has been performed "approximation free" numerically with accuracy control. For the few values needed here the long computing times (several minutes per value on a 150 MHz DEC-Alpha workstation) were acceptable.

Figure 17 displays the distance variation of the vdW free energy in terms of k_BT where $T = 300$ K as obtained from the parameters given in Table 8 as a function of the platelet distance l. The distance l_0 is the distance between the outer edges of the outermost slabs of the discrete model for the brushes. The energy diverges for $l_0 \to 0$; however, the typical size of a molecule establishes the lower limit l_0 may take, e.g., $l_0 > 0.5$ nm. At this limit the vdW interaction amounts to about 200 k_BT. Despite the tiny PEP fraction in the outer brush zones these contribute most to the interaction energy in a situation of near brush contact. The PE cores alone only account for considerably less than k_BT!

Since the outermost brush layers yield most of the interactive energies, the exact value of it depends somewhat on the discretization, because for a finer subdivision the outermost layers contain less PEP. The exact value of the interaction energy depends as well on the exact position of the main absorption peak and on the matching of the ω dependence of the dielectric functions. As an example, the model from which Figure 17 has been computed has been modified by shifting the value ω_{PEP} from the decane value down to ω_{PE} and up to 1.5×10^{17} s^{-1}. The oscillator strength f_{PEP} has been adjusted to match the observed index of refraction in each case. The result of these modifications results in a variation of the interaction energy from 35 to 68 to 102 k_BT at $l_0 = 1$ nm for the three ω_{PEP} values and from 107 to 220 to 336 k_BT at $l_0 = 0.5$ nm.

For the systems free energy to favor aggregation, the vdW interaction energy must be larger than the translational entropy loss $\Delta F_S = T\Delta S$ where ΔS is the entropy loss of a platelet due to aggregation. A reasonable estimate for an upper value of this entropy may be obtained by evaluating the textbook expression of the Sakur–Tetrode entropy of an ideal gas to yield the translation entropy S_t of a platelet.

$$S_t = k \ln\left(e^{(5/2)}\frac{(2\pi M k_B T)^{(3/2)}}{ch^3}\right) \tag{40}$$

where M is the platelet mass, c is the platelet concentration, and h is Planck's constant. The entropy difference between a single platelet coexisting with a stack of N platelets and one stack of N+1 platelets follow immediately:

$$\Delta S_t = k \ln\left(e^{5/2}\frac{(2\pi MkTN/(N+1))^{3/2}}{ch^3}\right) \tag{41}$$

With the data from Table 8 and the assumption of equal amounts of polymer in the core and in the brush zone a typical mass of $M = 2.5 \times 10^{-17}$ kg per platelet results, corresponding to 10^6 CH_2 units. With this weight per particle the particle density (concentration) in a 5% solution is $c = 2 \times 10^{18}$ m^{-3}. With these values the entropy contribution to the free energy due to attachment of one plate to a stack of $N = 5$ is

$$T\Delta S_t = 65\ kT \tag{42}$$

Free rotation—by again taking the textbook expressions for a free rotator—would contribute another 60k_BT. Both values are upper estimates: (i) the translational entropy contribution will be reduced by any internal degree of freedom of the aggregate; (ii) the rotational part will be diminished in more concentrated solutions by mutual obstruction of the platelets. The essence of the result is that the interaction energy must be about $10^2 k_BT$ in order to beat the entropy effects. The above figures for the vdW interaction show that this condition may be met, in spite of the fact that the absolute vdW energy amounts only to $f_{vdW} \approx 10^{-7}$–10^{-6} J/m^2.

The estimated strength of the vdW interaction can also be used, in order to rationalize the shear threshhold of $\dot\gamma \approx 500$ s^{-1} beyond which the aggregate system disintegrates. Given a shear rate $\dot\gamma$ the resulting stress s within the system becomes $s = \dot\gamma\eta$, where η denotes the shear transmitting viscosity in the system. The force parallel to the platelet plane trying to slide two aligned platelets of area A is then $F_s = sA = \dot\gamma\eta A$. On the other hand the vdW energy leads to a restoring force of $F_{vdW} = f_{vdW}b$, where b is the extension of the platelets perpendicular to the slide direction. With the observed alignment b is the short extension of the platelet planes. Disintegration will occur if F_s becomes comparable comparable to F_{vdW}. With the standard values used above one obtains $F_{vdW} = 5 \times 10^{-14}$–$5 \times 10^{-13}$ N. This has to be compared to the shear force $F_s \cong 10^{-12}$ N resulting from $\dot\gamma = 500$ s^{-1}, $A = 2.5 \times 10^{-12}$ m^2, and $\eta_{dec} = 0.84$ mPa s. Considering the order of magnitude estimates, the agreement is quite satisfactory.

Finally, one might wonder, why the platelets do not reassemble after removing the shear. We believe that the large shear gradient breaks up the very thin single platelets, thus reducing the large flat surface area necessary for the vdW interaction to be significant. Reassembling can only take place if the primary crystalline micelle re-forms again from the solution at high T.

6. Conclusion

We have presented a detailed study on the aggregation of diblock copolymers in solution where one of the blocks is able to crystallize. We have chosen the polyethylene–poly(ethylenepropylene) system which can be synthesized via an anionic route and subsequent hydrogenation. We have prepared a number of well-defined such diblocks varying both the molecular weights of the respective components and their degree of deuteration or hydrogenation. These diblock copolymers were dissolved in decane, in general using five different solvent scattering length densities. Most of the systems were investigated at a volume fraction $\Phi = 0.02$ by small angle neutron scattering. In some cases also concentration dependence studies were performed.

We found a complex hierarchy of structures involving length scales from about 3 to 5000 nm. The polyethylene component crystallizes in thin lamellar crystals with thicknesses ranging between 3 and 8 nm. They exhibit rather rough surfaces which can be understood from the tendency of polyethylene crystals to eject ethyl side branches which result from the 1,2 addition during the synthesis of the polybutadiene precursor polymer. These lamellae are surrounded by poly(ethylenepropylene) brushes with an average brush density profile close to parabolic, supporting thereby theoretical considerations on the basis of self-consistent field theories. Within the brush density fluctuations occur which are in accordance with what would be expected from blob scattering.

The thermodynamics behind the resulting morphology—core thickness and brush length as a function of the PE–PEP composition—was understood in terms of a free energy considering entropic contributions from brush stretching and enthalpic parts from the PE chain folding and defect incorporation. In terms of this approach various scaling relations between the different structural parameters were verified.

The very weak van der Waals interaction between the platelets leads to macroaggregation. Thereby, the large area of the platelets is essential—even a weak interaction integrated over a large surface is able to overcome the translational entropy. At low polymer volume fraction stacks of platelets with finite stacking number are observed. The organization of the platelets within one stack can be described by a paracrystalline structure factor. With increasing polymer volume fraction, the stacking number increases and at the same time the organization of the platelets within one stack gets better defined, leading to more pronounced structure factors.

Observation by a phase contrast microscope revealed needlelike shapes of the macroaggregates. Within these needles the polyethylene lamellae position themselves in the long direction. This result came from SANS studies on sheared samples. Finally, increasing the shear rate beyond a threshold of $\dot{\gamma} = 500\ \mathrm{s}^{-1}$, the aggregate structure is destroyed. The observed threshold shear rate agrees within reasonable accuracy with what can be calculated on the basis of the van der Waals attraction.

Note Added in Proof

At the time of the submission of this manuscript, a SANS work on similar polymers has been reported in *Macromolecules*: Lin, E. K.; Gast, A. P. *Macromolecules* **1996**, *29*, 4432.

Acknowledgment. We like to thank the National Institute for Standards and Technology, the Risø National Laboratory, the Institute Laue Langevin and the Laboratoire Léon Brillouin for providing beam time at their respective SANS machines and for the excellent hospitality during our stays.

References and Notes

(1) Halperin, A.; Tirell, M.; Lodge, T. P. *Adv. Polym. Sci.* **1992**, *100*, 31.
(2) Gast, A. P. *Scientific Methods for the Study of Polymer Colloids and Their Applications*; Kluwer Academic Publishes: Dordrecht, The Netherlands, 1990; pp 311−328.
(3) Tuzur, Z.; Kratochvil, P. *Advances in Colloid and Interface Science*; Elsevier: Amsterdam, 1976.
(4) Oranli, L.; Bahadur, P.; Riess, G. *Can. J. Chem.* **1985**, *63*, 2691.
(5) Bahadur, P.; Sastry, N. V.; Marti, S.; Riess, G. *Colloids Surf.* **1985**, *16*, 337.
(6) Gallot, Y.; Franta, P.; Rempp, P.; Benoit, H. J. *Polym. Sci., Part C* **1964**, *4*, 473.
(7) Kotaka, T.; Tanaka, T.; Hattori, M.; Inagaki, H. *Macromolecules* **1978**, *11*, 138.
(8) Periard, J.; Riess, G. *Eur. Polym. J.* **1973**, *9*, 687.
(9) Selb, J.; Gallot, Y. *Makromol. Chem.* **1980**, *182*, 1491.
(10) Higgins, J. S.; Dawkins, J. V.; Maghami, G. G.; Shakir, S. A. *Polymer* **1986**, *27*, 931.
(11) Plestil, J.; Baldrian, J. *Makromol. Chem.* **1975**, *176*, 1009.
(12) Bluhm, T. L.; Malhorta, S. L.; Hong, M.; Noolandi, J. *Polym. Prepr. (Am. Chem. Soc., Div. Polym. Chem.)* **1983**, *24*, 405.
(13) Iatrou, H.; Willner, L.; Hadjichristidis, N.; Halperin, A.; Richter, D. *Macromolecules* **1996**, *29*, 581.
(14) Morton, M.; Fetters, L. J. *Rubber Chem. Technol.* **1975**, *48*, 359.
(15) Roovers, J.; Toporowski, P. *Macromolecules* **1983**, *16*, 843.
(16) Crist, B.; Nicholson, J. C. *Polymer* **1994**, *35*, 1846.
(17) Gaucher, V.; Séguéla, R. *Polymer* **1994**, *35*, 2049.
(18) Tanzer, J. D.; Bartels, C. R.; Crist, B.; Graessly, W. W. *Maromolecules* **1984**, *17*, 2708.
(19) Almdal, K.; Koppi, K. A.; Bates, F. S.; Mortensen, K. *Macromolecules* **1992**, *25*, 1743.
(20) Duval, M.; Duplessix, R.; Picot, C.; Rempp, P.; Benoit, H.; Cotton, J. P.; Farnoux, B.; Ober, R. *J. Polym. Sci., Part B* **1976**, *14*, 585.
(21) Alexander, S. *J. Phys.* **1977**, *38*, 983.
(22) de Gennes, P. G. *Macromolecules* **1980**, *13*, 1069.
(23) Milner, S. T.; Witten, T. A.; Cates, M. E. *Macromolecules* **1988**, *21*, 2610.
(24) Hosemann, R.; Bagchi, S. N. *Direct Analysis of Diffraction by Matter*; North-Holland: Amsterdam, 1962.
(25) de Gennes, P. G. *Scaling Concepts in Polymer Physics*; Cornell University Press: Ithaca, NY, 1979.
(26) Auroy, Ph.; Auvray, L.; Leger, L. *Physica A* **1991**, *172*, 269.
(27) Dozier, W. D.; Huang, J. S.; Fetters, L. J. Macromolecules **1991**, *24*, 2810.
(28) McConnell, G. A.; Gast, A. P.; Huang, J. S.; Smith, S. D. *Phys. Rev. Lett.* **1993**, *71*, 2102.
(29) Monkenbusch, M.; Schneiders, D.; Richter, D.; Farago, B.; Fetters, L. J.; Huang, J. S. *Physica B* **1995**, *213* & *214*, 707.
(30) Monkenbusch, M.; Schneiders, D.; Richter, D.; Farago, B.; Fetters, L. J.; Huang, J. S. *Il Nuovo Cimento* **1994**, *16*, 747.
(31) Lindner, P.; Oberthür, R. *Physica B* **1989**, *156* & *157*, 410.
(32) Mortensen, K.; Brown, W.; Nordén, B. *Phys. Rev. Lett.* **1992**, *68*, 2340.
(33) McConnell, G. A.; Lin, M. Y.; Gast, A. P. *Macromolecules* **1995**, *28*, 6754.
(34) Vilgis, T.; Halperin, A. *Macromolecules* **1991**, *24*, 3321.
(35) Elias, H. G. *Makromoleküle*; Hüpf + Wepf-Verlag: Basel, 1990; p 753.
(36) Parsegian, V. A.; Ninham, B. W. *J. Theor. Biol.* **1973**, *38*, 101−109.
(37) See chapters 2 and 3 in: Mahanty, J.; Ninham, B. W. *Dispersion Forces*; Academic Press: London, New York, San Francisco, 1976.
(38) Batzer, H., Ed. *Polymere Werkstoffe*; Thieme: Stuttgart, 1972.
(39) Table 3.2 in ref 37.

MA961039K